Improved modeling of spherical-wave AVO

Charles P. Ursenbach, Arnim B. Haase, and Jonathan E. Downton*

ABSTRACT

Spherical-wave reflection coefficients, which are vital in modeling supercritical reflections, are considerably more difficult to calculate than their plane-wave analogues. We seek to narrow this gap by performing one of the requisite integrations analytically. The key is to assume a wavelet of the Rayleigh form. The resulting reflection coefficients are accurate, even if the true wavelet is not a Rayleigh wavelet, as long as one follows a simple prescription for choosing the wavelet parameters. The method is also efficient enough to implement in an interactive program, and is thus promising for use in high-volume, supercritical modeling.

INTRODUCTION

The motivation to carry out spherical-wave AVO modeling is rooted in the rich potential of long-offset amplitudes. Long offsets are key to obtaining density information from AVO analysis (Wang, 1999) and help to clarify interpretation of Class I amplitudes (Hilterman et al., 2000). However, long offset data introduce additional challenges to AVO inversion. For instance NMO stretch and offset-dependent tuning become substantial at wide angles, necessitating the use of waveform inversion (Downton, 2005). Anisotropic moveout is also more pronounced at long offsets. In addition to these problems, wide angle data can traverse a critical angle, and this introduces anomalously large amplitudes. Downton and Ursenbach (2006) have presented a method for AVO inversion of supercritical amplitudes, but this relies on an accurate theory of supercritical reflectivities. The shortcomings of the plane-wave Zoeppritz reflectivities near the critical angle are well-known, e.g. (Haase, 2004a; van der Baan and Smit, 2006), and spherical-wave reflectivities are required to correctly represent behavior in this region and to make available the full value of long-offset data.

Two paradigms currently exist for the calculation of reflected spherical waves, namely, harmonic and impulsive. The theory for the harmonic source is credited to Lamb (1904) and Sommerfeld (1909) and is described in standard texts, e.g. Aki and Richards (1980); there is also evidence of its use in exploration seismology (MacDonald et al., 1987). The theory for the impulsive source was pioneered by Cagniard (1939) and has been developed by Bortfeld (1962), Tygel and Hubral (1984) and Hubral and Tygel (1985). Thus two general approaches exist, but neither has found extensive application in practical problems.

The principal obstacle to the use of these methods is computational burden. Seismic wavelets are neither monochromatic nor spikelike, but are bandlimited. Thus appropriate reflectivities require either calculation for a range of monofrequency wavelets, followed by inverse Fourier transformation with the wavelet, or calculation of impulsive results for a number of time lags, followed by convolution with the wavelet. The former approach has

*Veritas DGC

been realized as a practical scheme (Haase, 2004a), but both approaches require extensive computations, and one wonders if a more efficient approach is possible.

Of course it is tempting to look for approximations, but these must honor behavior in the critical region in order to address the applications described above. Krail and Brysk (1983) developed an approximation to the spherical-wave potential (equation 1 below) consisting of a series expansion in $1/(kr)$, where k is the wavenumber and r is the distance from the source. In addition they replace the plane-wave coefficient and the Bessel function of the integrand by Taylor series expansions. Furlong et al. (1994) developed a somewhat different approximation that consists of assuming that the reflected and transmitted waves are spherical (or dipolar for converted waves). The reflection coefficients are then obtained by matching boundary conditions across the interface. Both of these approximations may be reasonable for small angles and may be of value in near-surface studies, but both rest upon assumptions that are not appropriate in the vicinity of critical angles.

The method proposed in this paper is designed to substantially reduce the time requirements for spherical-wave reflection coefficient calculations, while still maintaining accuracy in the critical region. It is based on three approximations:

- The wavelet is assumed to be of a particular form which allows for analytical integration over frequency. By introducing the wavelet at the outset one avoids an entire layer of numerical integrations.
- The arrival time at the receiver is assumed to be equal to that predicted by ray theory, which further reduces the number of numerical integrations.
- The wave displacement is assumed to be directed along the raypath. This reduces the displacement from a vector to a scalar.

We will first derive a method based on these approximations. We will then investigate the effect of each approximation and perform timing tests to show that the method is both accurate and efficient.

THEORETICAL DEVELOPMENT

A fundamental model in exploration seismology is that of P-wave reflections in a two-layer elastic model, illustrated in Figure 1. The *plane-wave* reflection coefficient for this system is the well-known Zoeppritz expression, $R_{\mathrm{PP}}(p;\alpha_1,\beta_1,\rho_1;\alpha_2,\beta_2,\rho_2)$, where p is a ray parameter (the horizontal P-wave slowness), α, β, and ρ are P-wave velocity, S-wave velocity, and density, and subscripts 1 and 2 refer to upper and lower media. The *generalized* reflection coefficient associated with spherical waves, which includes contributions from both reflected and head waves, can be given as an integral over $R_{\mathrm{PP}}(p)$. The fundamental theory is well-established, and it is given in detail, for example, by Aki and Richards (1980). They express the spectrum of the displacement potential as a weighted integral over all ray parameters of cylindrical waves times plane-wave reflection coefficients. In analogy with their equation 6.30 for free surface reflections, the pertinent expression for P-wave

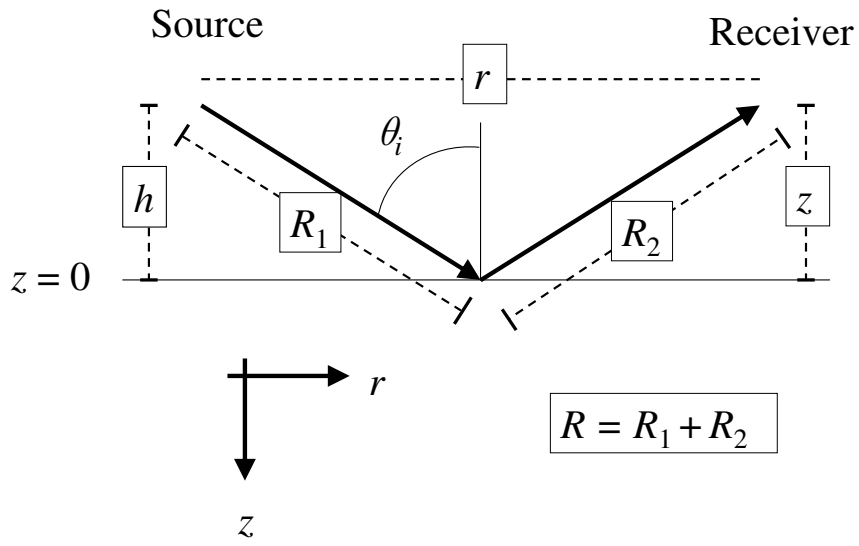

FIG. 1. Schematic of the two-layer model investigated in this study.

reflections from a solid-solid interface can be derived as

$$\phi(\omega) = Ai\omega e^{-i\omega t} \int_0^\infty R_{\mathrm{PP}}(p;\alpha_1,\beta_1,\rho_1;\alpha_2,\beta_2,\rho_2)\frac{p}{\xi_1}J_0(\omega pr)e^{i\omega\xi_1(z+h)}dp. \qquad (1)$$

Here A is a scaling factor, ω is the frequency (assumed positive in the derivation), t is time, ξ_1 is the vertical P-wave slowness in the upper layer, J_0 is the zero-order Bessel function, $(0,0,h)$ is the source position, r is the radial receiver coordinate, and z is the vertical receiver coordinate.

The displacement is obtained by applying a gradient in the receiver position to the above potential. Weighting by the wavelet and applying an inverse Fourier transform yields the time trace observed at the receiver. One way to obtain AVO information from this trace is to extract the maximum of the trace envelope. This method has been implemented by Haase (2002, 2003, 2004a), and we refer to it as the *numerical method*, to distinguish it from the method of this paper.

The first step in developing the *semi-analytical method* of this paper is to interchange the order of frequency and ray-parameter integrations, and then to choose a wavelet which allows one of these, the frequency integration, to be carried out analytically.

Analytic integration over ω

Using the spectrum of the potential, equation 1, we write the time-dependent potential as

$$\Phi(t) = \int_{-\infty}^{\infty} w(\omega)\phi(\omega)d\omega, \tag{2}$$

where $w(\omega)$ is the wavelet and we require it to be of the following form:

$$w(\omega) \propto |\omega|^n \exp(-n|\omega|/\omega_0), \qquad n = 1, 2, 3, \ldots, \qquad 0 < \omega_0 < \infty. \tag{3}$$

This wavelet has been discussed in a seismic context (Hubral and Tygel, 1989) and we refer to it as the Rayleigh wavelet of order n. Its maximum amplitude occurs at ω_0.

Equation 2 involves integration over both positive and negative frequencies. However it is advantageous to change the lower bound of the ω-integration to zero and multiply by a factor of two. This yields the analytic or complex potential, $\Phi^c(t)$, whose real part is equal to the original integral (see Kanasewich (1973), eqn. 11.9.14). We will require the analytic trace later, so this is a convenient step to obtain it more directly. Substituting equations 1 and 3 into equation 2 (with a modified lower bound) we then interchange the order of p and ω integrations*, as shown here:

$$\begin{aligned}
\Phi^c(t) &= 2\int_0^\infty \omega^n e^{-n\omega/\omega_0} \left\{ Ai\omega e^{-i\omega t} \int_0^\infty R_{\text{PP}}(p)\frac{p}{\xi_1} J_0(\omega p r)\exp[i\omega\xi_1(z+h)]dp \right\} d\omega \\
&= 2Ai\int_0^\infty R_{\text{PP}}(p) \left\{ \int_0^\infty \omega^{n+1} J_0(\omega p r) e^{-\omega\{(n/\omega_0)+i[t-\xi_1(z+h)]\}} d\omega \right\} \frac{p}{\xi_1} dp \qquad (4) \\
&\equiv 2Ai\int_0^\infty R_{\text{PP}}(p) I(p, \xi_1(p), r, z, h, t, n, \omega_0)\frac{p}{\xi_1} dp
\end{aligned}$$

In the last step we define $I(p, \xi_1, r, z, h, t, n, \omega_0)$ as the result of integration over ω. Changing the lower bound to zero also gives this integral the form of a Laplace transform, and an analytic solution is available (Erdelyi, 1954):

$$I = \frac{(n+1)!}{\tau^{n+2}} P_{n+1}\left(\frac{T}{\tau}\right), \tag{5}$$

$$T = \frac{n}{\omega_0} + i(t - \xi_1[z+h]), \tag{6}$$

$$\tau = \sqrt{T^2 + p^2 r^2}, \tag{7}$$

where $P_n(x)$ is a Legendre polynomial.

Calculation of the gradient

Next we apply a gradient with respect to receiver position in order to obtain the displacement. If we assume that displacement is in the direction of propagation of the reflected

*Bortfeld (1962) justifies changing the order of integration for this integral. He develops a method in which a sinc function wavelet is employed for the integration over frequency, and the actual seismic wavelet is introduced at the end of the procedure by convolution. His method is therefore more general than the present approach, but also more computationally intensive.

wave, then we can begin by substituting $r = R\sin\theta_i$ and $z + h = R\cos\theta_i$ (see Figure 1). A directional derivative is then obtained by taking a simple derivative with respect to R. We use a $\|$-subscript to indicate displacement parallel to the ray direction:

$$u^c_{\|}(t) = \frac{\partial \Phi^c(t)}{\partial R} = 2Ai \int_0^\infty R_{\rm PP}(p) \left(\frac{\partial I}{\partial R}\right) \frac{p}{\xi_1} dp, \tag{8}$$

$$\begin{aligned} \frac{\partial I}{\partial R} &= -\frac{(n+2)!}{\tau^{n+3}} P_{n+1}\left(\frac{T}{\tau}\right) \frac{\partial \tau}{\partial R} \\ &\quad + \frac{(n+1)!}{\tau^n} \frac{n+1}{\tau^2 - T^2} \left[P_n\left(\frac{T}{\tau}\right) - \frac{T}{\tau} P_{n+1}\left(\frac{T}{\tau}\right)\right] \frac{\partial}{\partial R}\left(\frac{T}{\tau}\right), \end{aligned} \tag{9}$$

$$\frac{\partial T}{\partial R} = -i\xi_1 \cos\theta_i, \tag{10}$$

$$\frac{\partial \tau}{\partial R} = \frac{-i\xi_1 T \cos\theta_i + Rp^2 \sin^2\theta_i}{\tau}. \tag{11}$$

The quantity $u^c_{\|}$ thus represents the analytic trace. We should bear in mind that the assumption regarding the direction of displacement of the reflected wave may not be valid in the vicinity of the critical point, where it cannot be distinguished from the head wave. However, the directional difference in this region is small, and results below show the assumption to be reasonable.

Reflected-wave amplitude

The complex displacement of equation 8 is given as a function of time, t. Let us assume that the signal of interest will arrive at the receiver at time R/α_1. (The discussion regarding the direction-of-displacement assumption applies here as well.) Let us set $t = R/\alpha_1$ (note that this must be done only *after* applying the gradient). The result of this is an estimate of the maximum amplitude of the reflected wave, which contains information on the reflection coefficient. It is given by equations 8-11, but with the quantity T replaced by

$$T_0 = n/\omega_0 + i(R/\alpha_1 - \xi_1[z+h]), \tag{12}$$

and with all derivatives changed from $\frac{\partial}{\partial R}$ to $\frac{\partial}{\partial R}\big|_{T=T_0}$, emphasizing that evaluation of t occurs *after* application of the derivative.

Changing the variable of integration

Collecting the above results together, the reflected spherical-wave complex displacement is given by the integral

$$u^c_{\|}(t = R/\alpha_1) = 2Ai \int_0^\infty R_{\rm PP}(p; \alpha_1, \beta_1, \rho_1, \alpha_2, \beta_2, \rho_2) \left.\frac{\partial I}{\partial R}\right|_{T=T_0} \frac{p}{\xi_1} dp. \tag{13}$$

Because p and ξ_1 satisfy the relation $(p\alpha_1)^2 + (\xi_1\alpha_1)^2 = 1$, it is acceptable to define $\sin\theta \equiv p\alpha_1$ and $\cos\theta \equiv \xi_1\alpha_1$. In the following numerical implementation it is more convenient to

use $\cos\theta$ as the integration variable so a change of variables is performed. First we note that $(p/\xi_1)dp = \tan\theta d(\sqrt{1-\cos^2\theta}/\alpha_1) = -d(\cos\theta)/\alpha_1$. Next the integration range is divided into two parts: $\int_0^\infty \cdots dp = \left[\int_0^{1/\alpha_1} + \int_{1/\alpha_1}^\infty\right] \cdots dp$. Under the change of variables this becomes $\left[\int_1^0 + \int_{i0}^{i\infty}\right] \cdots d(\cos\theta)$, so that equation 13 is expressed as

$$u_\parallel^c(t = R/\alpha_1) = 2A\left[\int_0^1 - \int_{i0}^{i\infty}\right] R_{\mathrm{PP}}(\theta)\left(\frac{i}{\alpha_1}\frac{\partial I}{\partial R}\bigg|_{T=T_0}\right) d(\cos\theta). \tag{14}$$

Normalization

Spherical waves decrease in amplitude with distance traveled, while plane waves do not. This complicates comparison of reflection coefficients. It is desirable to remove the spherical divergence and near-field effects and to thus isolate the effect on amplitude of reflection alone. One simple approach is to normalize the spherical-wave result by the result that would be obtained if the reflection coefficient were set to unity. Setting $R_{\mathrm{PP}} = 1$ in the spherical-wave potential (equation 1) allows the integral over p (the Sommerfeld integral) to be performed analytically, recovering the spherical-wave potential in a homogeneous medium,

$$\phi^{\mathrm{hom}}(\omega) = \frac{A}{R}\exp\left[-i\omega\left(t - \frac{R}{\alpha_1}\right)\right]. \tag{15}$$

Taking the derivative with respect to R, setting $t = R/\alpha_1$, weighting by the wavelet, and then finally integrating over the positive frequencies and multiplying by two yields the homogeneous analogue of equation 14,

$$u_\parallel^{c,\mathrm{hom}}(t = R/\alpha_1) = 2A\left[-\left(\frac{\omega_0}{n}\right)^{n+1}\frac{n!}{R^2} + i\left(\frac{\omega_0}{n}\right)^{n+2}\frac{(n+1)!}{\alpha_1 R}\right]. \tag{16}$$

Dividing equation 14 by equation 16 gives a normalized reflection coefficient suitable for comparison with the plane-wave result. If equation 16 is incorporated earlier, by dividing it into the weighting function, $2A(i/\alpha_1)(\partial I/\partial R)|_{T=T_0}$, then a normalized weighting function results, the real part integrating to one, and the imaginary part to zero. We will denote this

$$W_n = \frac{\frac{i}{\alpha_1}\frac{\partial I}{\partial R}\Big|_{T=T_0}}{-\left(\frac{\omega_0}{n}\right)^{n+1}\frac{n!}{R^2} + i\left(\frac{\omega_0}{n}\right)^{n+2}\frac{(n+1)!}{\alpha_1 R}} \tag{17}$$

with

$$\left[\int_0^1 - \int_{i0}^{i\infty}\right] W_n(\theta, \theta_i, \omega_0, R, \alpha_1)d(\cos\theta) = 1 + 0i. \tag{18}$$

We can then write the ratio of equation 14 and equation 16 as a *spherical-wave reflection coefficient*:

$$R_{\mathrm{PP}}^{\mathrm{sph}}(\theta_i) = \left[\int_0^1 - \int_{i0}^{i\infty}\right] R_{\mathrm{PP}}(\theta)W_n(\theta, \theta_i, \omega_0, R, \alpha_1)d(\cos\theta), \tag{19}$$

where $W_n(\theta, \theta_i)$ acts as a weighting function to transform $R_{\mathrm{PP}}(\theta)$ to $R_{\mathrm{PP}}^{\mathrm{sph}}(\theta_i)$.

A connection can be drawn between this normalization and current processing practice. The two terms in the normalization factor, equation 16, correspond to near-field and far-field effects respectively. If one eliminates the near-field term, then normalization is equivalent to a spherical divergence correction. In this case equation 18 would not hold perfectly, but for the models considered in this study the error is negligibly small. This can be understood by noting that the ratio of the near-field and far-field terms is $i\frac{n}{n+1}S$, where $S \equiv \alpha_1/(R\omega_0)$, a quantity indicating the importance of spherical effects. For a monochromatic wavelet, the quantity controlling the size of spherical effects is $\alpha_1/(R\omega)$ (also written $1/(kr)$ in the introduction). It is therefore reasonable that the quantity S arises naturally in this theory. Because the two terms are 90° out of phase, the fractional change in magnitude from neglecting the near-field is on the order of S^2. This is negligible except in near-surface studies. Thus, although the calculations below all use W_n as given by equation 17, essentially identical results would have been obtained using the approximation

$$W_n \approx \left(\frac{n}{\omega_0}\right)^{n+2} \frac{R}{(n+1)!} \left.\frac{\partial I}{\partial R}\right|_{T=T_0}. \tag{20}$$

Simplified expressions for W_n

The previous section is key to producing our final results. We have defined the quantity S, and it turns out that after normalization all dependence on R, ω_0 and α_1 is via this combined quantity, so that equation 19 can be rewritten as

$$R_{\mathrm{PP}}^{\mathrm{sph}}(\theta_i) = \left[\int_0^1 - \int_{i0}^{i\infty}\right] R_{\mathrm{PP}}(\theta) W_n(\theta, \theta_i, S) d(\cos\theta). \tag{21}$$

This can be demonstrated by working out an explicit expression for W_n:

$$\begin{aligned}
W_n &= -\frac{(nS)^{n+2}}{\overline{\tau}^{n+4}} \frac{BP_n(\overline{T}/\overline{\tau}) + CP_{n+1}(\overline{T}/\overline{\tau})}{1 + iSn/(n+1)}, && (22)\\
B &= (n+1)(i+nS)\overline{\tau}, && (23)\\
C &= -n^2(1+n)S^2 - inS[2(n+1) + \cos\theta\cos\theta_i] \\
&\quad + n(\sin^2\theta + \sin^2\theta_i) + 3(1 - \cos\theta\cos\theta_i) - 2(\cos\theta - \cos\theta_i)^2, && (24)\\
\overline{\tau} &= \sqrt{T^2 + \sin^2\theta\sin^2\theta_i}, \\
&= \sqrt{(nS)^2 + 2inS(1 - \cos\theta\cos\theta_i) + (\cos\theta - \cos\theta_i)^2}, && (25)\\
\overline{T} &= nS + i(1 - \cos\theta\cos\theta_i). && (26)
\end{aligned}$$

Equations 21-26 together form the central theoretical result of this paper. They provide the machinery for efficient calculation of spherical-wave reflection coefficients.

We can now see explicitly that W_n depends only on $\cos\theta$, $\cos\theta_i$, and S. This is obviously convenient for the numerical integration over $\cos\theta$ in equation 21. Quantities which affect the magnitude of spherical effects are combined in the dimensionless quantity $S = \alpha_1/(R\omega_0)$. Spherical effects increase with increasing velocity in the overburden ($\alpha_1 \uparrow$),

decreasing distance traveled by the wavelet ($R\downarrow$), and decreasing dominant frequency of the wavelet ($\omega_0\downarrow$). Thus increasing S corresponds to increasing spherical effects.

We can also show that in the limit of *decreasing* S the weighting function must act as a delta function, i.e., $\lim_{S\to 0} W_n(\theta,\theta_i,S) = \delta(\cos\theta - \cos\theta_i)$. (See Appendix A for details.) In this limit then the normalized spherical-wave reflection coefficient approaches the plane-wave Zoeppritz coefficient (see equation 21).

Calculation examples

The W_n expression has been implemented for numerical computation (MATLAB and Java). We present computational results below for $1 \le n \le 8$, as this range is generally adequate to model the frequency content of a seismic wavelet.

Cross-sections of W_4 are shown in Figure 2 below. The function is peaked for values of θ near θ_i, and becomes narrower at larger angles, corresponding to longer raypaths. These facts accord with the delta function limit described above. Thus the $\cos\theta$-integration in equation 21 can be restricted to a compact range.

The result of equation 21, the normalized spherical reflection coefficient, is illustrated in Figure 3 (dotted line). This is compared to the plane-wave reflection coefficient in the integrand whose absolute value is shown as a solid line. Thus the plane-wave reflection coefficient (solid line) is weighted by functions such as those in Figure 2 and integrated to yield points on the normalized spherical-wave reflection coefficient curve (dotted line). Both the amplitude and phase of the spherical wave results differ strongly from the plane-wave result near the critical angle. This is observed even at 2000 m (Haase, 2004a). Thus spherical waves should be considered for any quantitative treatment of supercritical reflections.

Table 1. Two-layer, elastic interface model employed in calculations.

	Density (kg/m^3)	P-wave velocity (m/s)	S-wave velocity (m/s)
Layer 1	2400	2000	879.88
Layer 2	2000	2933.33	1882.29

Details of implementation

Two types of calculation are carried out in this study, the fully numerical approach of Haase (2004a), and the semi-analytical method of equation 21, in which the frequency integration has already been performed analytically.

To carry out the remaining numerical integration in equation 21 it is convenient to replace $S = \alpha_1/(R\omega_0)$ with $S_z \equiv S/\cos\theta_i$, where $S_z = \alpha_1/[(z+h)\omega_0]$, or, for the case of $h = z$ which we will consider here, $S_z = \alpha_1/(2z\omega_0)$. S depends on the angle of incidence, while S_z depends only on the model and the wavelet, and is thus constant for a given reflection coefficient curve. It is also convenient to deal with $f(=\omega/2\pi)$ rather than ω.

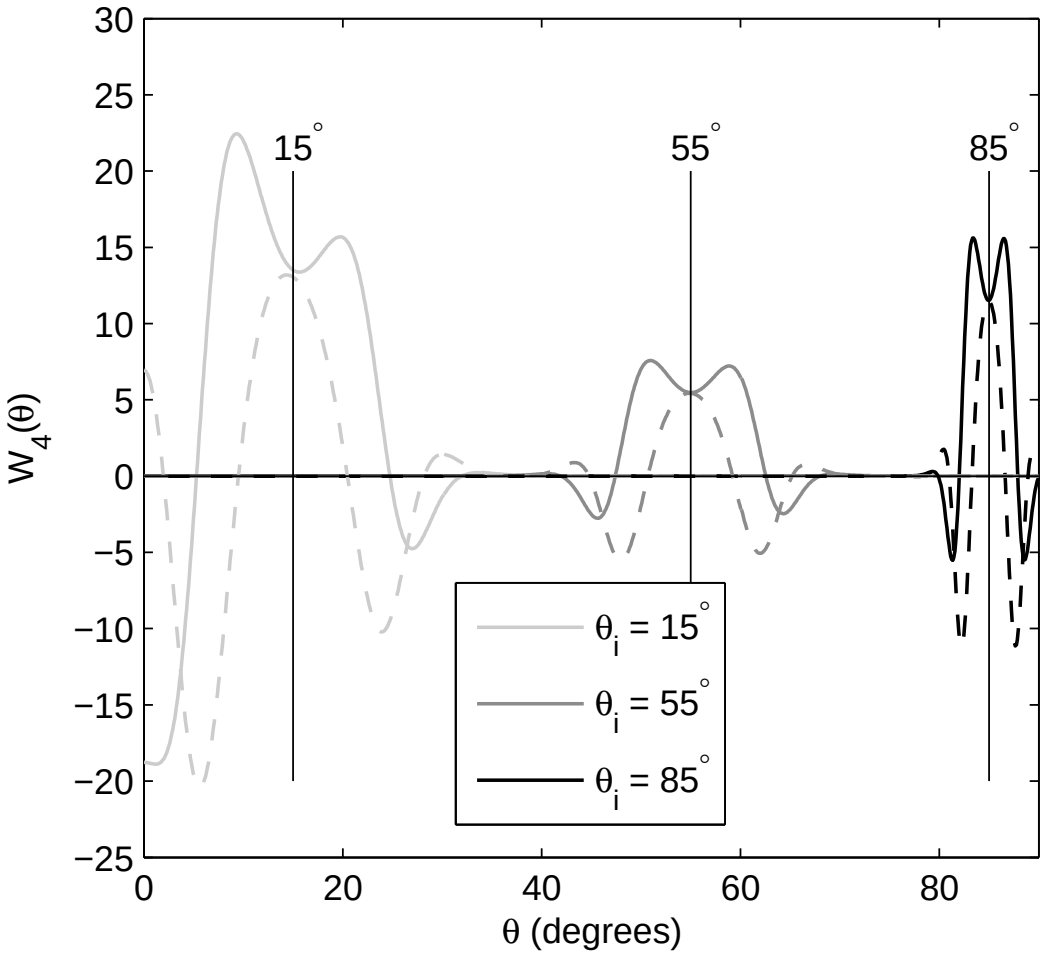

FIG. 2. Some of the weighting functions (i.e., equation 17) used in evaluating equation 21, the spherical-wave reflection coefficient, for a given angle of incidence, θ_i. The wavelet is of the form of equation 3, with n = 4, $\omega_0 = 200$ s^{-1} (or $f_0 \equiv \omega_0/2\pi \approx 31.83$ Hz), α_1 = 2000 m/s, and $z = h$ = 500 m, so that S = 0.01. The weighting functions shown here are for incidence angles of 15°, 55°, and 85°. In each case both the real component (solid line) and the imaginary component (dashed line) of the function are peaked near the angle of incidence.

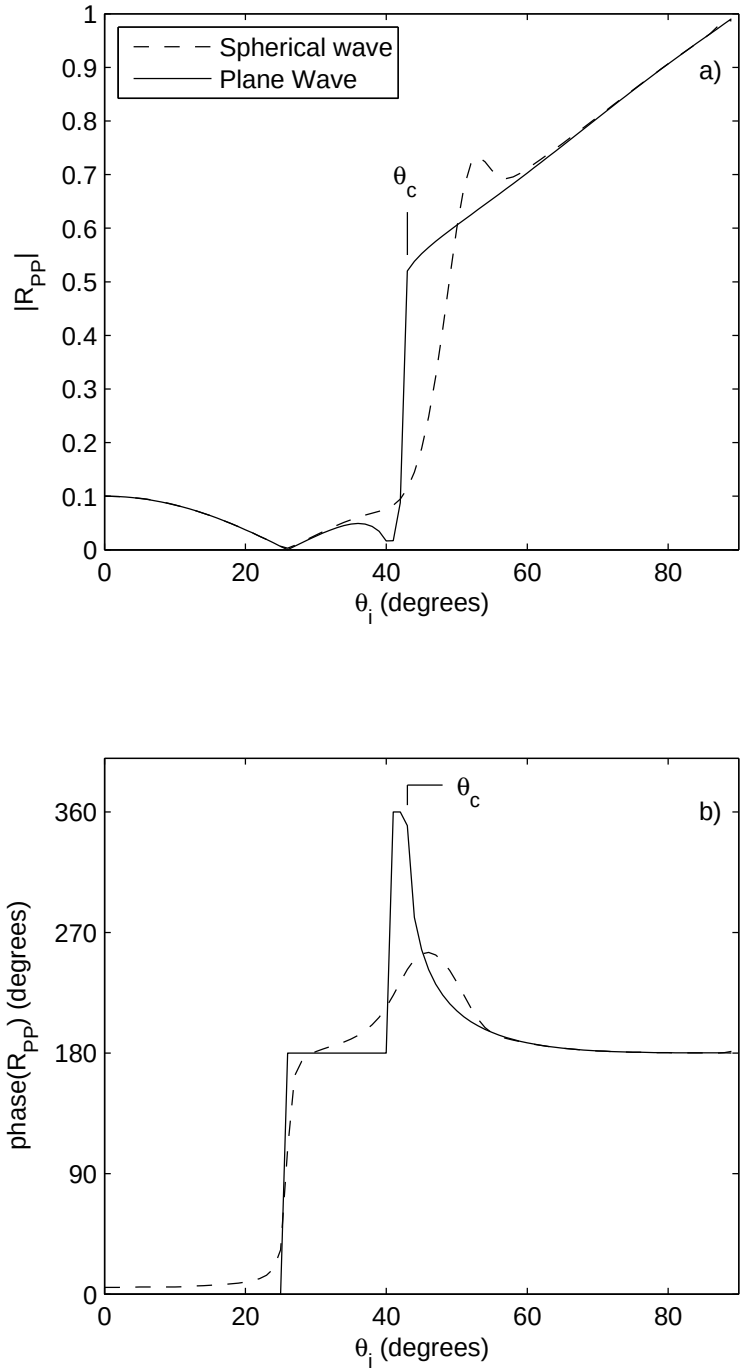

FIG. 3. Comparison of the a) magnitude and b) phase of plane wave and spherical-wave reflection coefficients for the Class I AVO parameters of Table 1. Other parameters are as given in Figure 2. The symbol θ_c denotes the critical angle. Values of the spherical-wave reflection coefficients at $\theta_i = 15°, 55°$, and $85°$ were calculated using the weighting functions displayed in Figure 2.

Our inputs therefore consist of 1) earth parameters, 2) angle of incidence, 3) n and S_z, and 4) parameters controlling the numerical integration. For a simple scheme, the numerical integration parameters consist of the grid width and the upper cutoff for the imaginary path (which formally is $i\times\infty$). In the calculations below we have chosen $|\Delta(\cos\theta)| = 0.001$ and $(\cos\theta)_{\max} = 0.1i$, unless otherwise noted. Neither decreasing the grid width nor increasing the cutoff produces any visible change to the plots.

TESTING OF THE METHOD

To be of value, this new method of calculating the spherical-wave reflection coefficient (equations 21-26) must be both accurate and efficient. In this section we estimate the effect of each of the three approximations employed in the derivation, while timing measurements will be used to estimate the efficiency.

Description of model

Table 1 contains earth parameters specifying a Class I AVO system with a critical point at $\sim 43°$. Following Haase (2004a) we also employ depths of $z = h$ = 500 m, and an overburden P-wave velocity of α_1 = 2000 m/s (see Table 1 above), unless otherwise noted. This information, together with f_0, completely specifies S_z, which then determines the deviation from plane wave behavior for a Rayleigh wavelet of order n.

Test of arrival time approximation

Aside from numerical errors, the arrival time approximation is the only source of difference between this method and the fully numerical method of Haase (2004a), if the same wavelet is used in both methods. Figure 4 below displays the difference $|R_{\rm PP}^{t-\max}| - |R_{\rm PP}^{t-\rm ray}|$ when a wavelet of the Rayleigh form (equation 3) is used in both the numerical and semi-analytical methods. The fully numerical approach (Haase, 2004a) estimates the arrival time from the maximum of the trace envelope, while the semi-analytical method assigns the arrival time $t = R/\alpha_1$. The largest deviation occurs just past the critical angle, where the reflected wave and head wave are separating from one another. Even here though the difference is small, and we conclude that this approximation introduces negligible error.

Test of travel path approximation

This approximation is present in the method of Haase (2004a) as well. It arises from extracting the component of the gradient along the raypath, and neglecting any displacement perpendicular to it. To estimate the effect of this approximation, the numerical procedure of Haase (2004a) was modified to extract only the perpendicular component instead of the parallel component. This "perpendicular" reflection coefficient is shown in Figure 5. The largest value again occurs just past the critical angle, and is again negligibly small. As with the travel time approximation, the errors appear in the region where reflecting and head waves are separating.

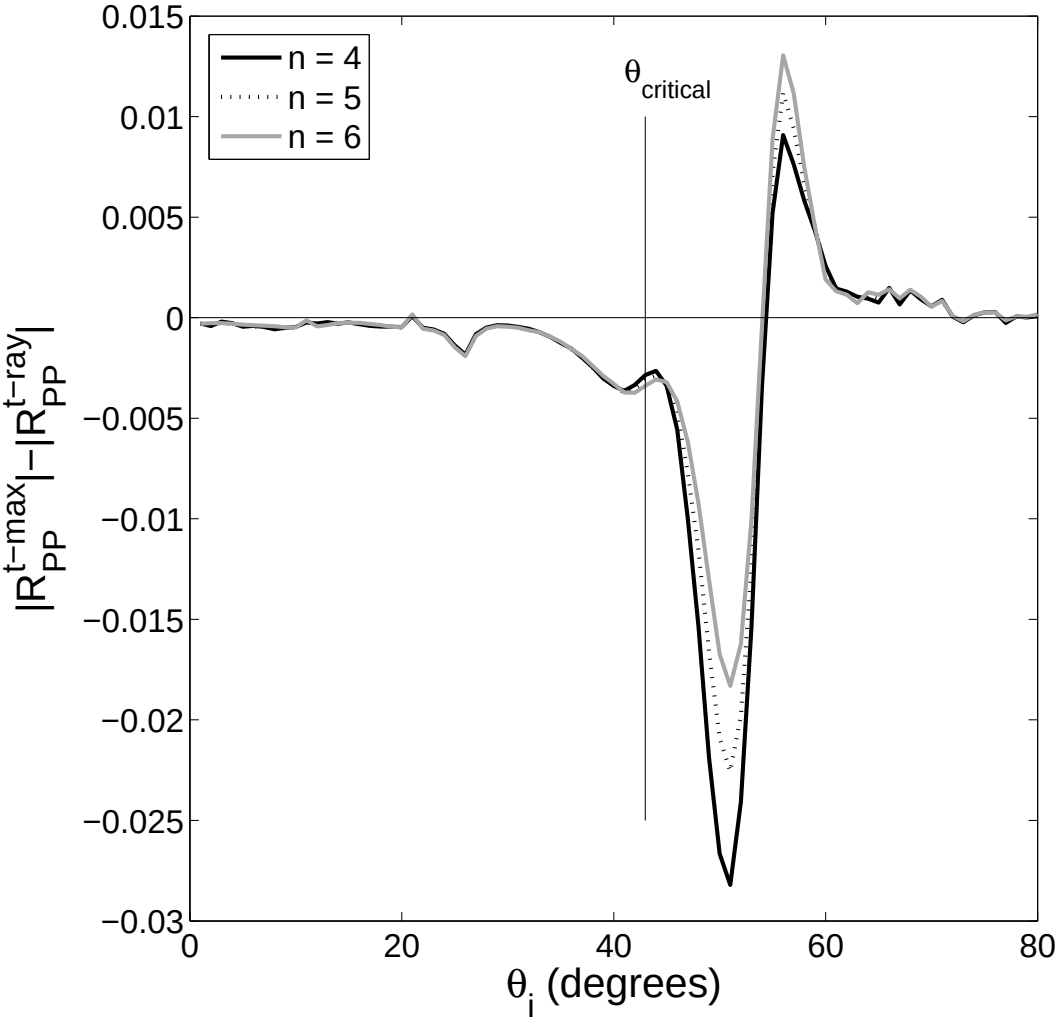

FIG. 4. The difference between spherical-wave reflection coefficients calculated by different methods. One method calculates the zero-phase arrival time by locating a maximum in the trace. The other method calculates the arrival time from ray theory with $t = R/\alpha_1$. The largest differences occur just past the critical angle, as reflected waves and head waves are separating to become distinct entities. Even here the differences are small (note the vertical scale). When reflection coefficient curves for the two methods are plotted together, they are both similar in appearance to the dotted line in Figure 3a, and are nearly indistinguishable from one another.

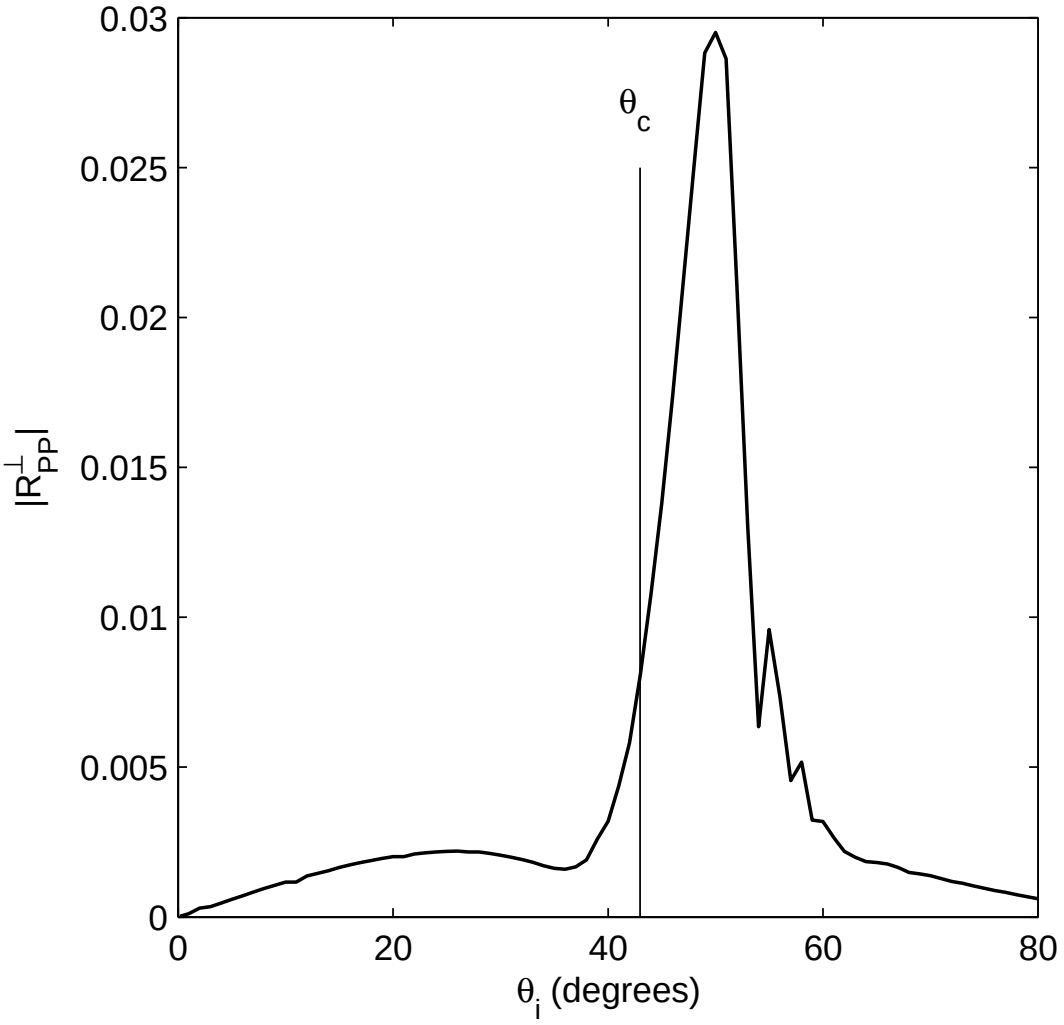

FIG. 5. The spherical-wave reflection coefficient calculated using only the displacement perpendicular to the raypath. All other calculations in this study use the component parallel to the raypath. This figure provides a measure of the error of the parallelity assumption. The calculation was performed using a 5/15-80/100 Hz Ormsby wavelet with z = 500 m. Note the vertical scale.

Test of wavelet approximation

There are no further approximations in this method if the Rayleigh wavelet (equation 3) is used in modeling. Indeed this is one reason, among others (Hubral and Tygel, 1989), to increase the use of Rayleigh wavelets in exploration geophysics. However, the zero-phase Ormsby and Ricker wavelets are currently more widely used, and it is of interest to know how well Rayleigh reflection coefficients will represent the reflection behavior of these more common wavelets. We show that there are simple prescriptions for f_0 and n which allow the zero-phase Rayleigh wavelet to be used to mimic the reflection behavior of Ormsby and Ricker wavelets.

Fundamental wavelet parameters

It is first useful to reduce the number of parameters used to describe wavelets. It was noted in the Theory section that the Rayleigh reflection coefficient curve depends on only two variables, n and S_z, where $S_z = \alpha_1/(4\pi z f_0)$. It can be shown, empirically at least, that the Ormsby curve depends primarily on two variables as well, and that the Ricker curve depends on only one variable.

Figure 6 displays the Ormsby reflection coefficient curve for six models in which $\overline{S}_z = 1/50$, where $\overline{S}_z \equiv \alpha_1/(4\pi z \overline{f})$ and $\overline{f}$ is the average frequency of the Ormsby wavelet (see Appendix B). For the most part the six lines are roughly coincident, showing that the average frequency is a fundamental parameter describing reflectivity of the Ormsby wavelet. (Note that in the case of curves for which the value of α_1 differs from that in Table 1, all other velocities have been scaled as well so that the plane-wave Zoeppritz coefficients are unchanged.) Oscillations are present around the critical angle, which is typical of Ormsby wavelet calculations (Haase, 2004a), and the inset shows these in greater detail. There the curves are grouped into three pairs of strongly coincident lines. Inspection of the wavelet definitions in the legend reveals that each pair possesses a common value of $(f_1 + f_2)/(f_3 + f_4)$, which we represent by the symbol B_r. Thus the Ormsby $R_{\mathrm{PP}}^{\mathrm{sph}}$ is primarily determined by $\overline{S}_z$ and B_r.

The Ormsby wavelet is defined by four frequencies, and two combinations of these, the average frequency and the upper-to-lower band edge ratio, have been described. The remaining information pertains to definition of the tapers at each band edge. Figure 7 displays $R_{\mathrm{PP}}^{\mathrm{sph}}$ for three Ormsby wavelets which all have similar $\overline{S}_z$ and B_r but which differ in their taper definitions. The first is a 10/10-90/90 boxcar filter, the second is a more conventional linearly tapered 5/15-80/100 Ormsby wavelet (also displayed in Figure 6), and the third is the same as the second but with a cosine taper. There is little difference among the resulting reflection coefficient curves, so we conclude that the taper definition has little influence on $R_{\mathrm{PP}}^{\mathrm{sph}}$ for the Ormsby wavelet.

The zero-phase Ricker wavelet has only one adjustable parameter, f_0, and is given as

$$w_{\mathrm{Ricker}}(f) = f^2 \exp\left[-(f/f_0)^2\right]. \tag{27}$$

It has been criticized in some quarters (Hosken, 1988), but is still in common use. Calculations (not shown) demonstrate that the Ricker $R_{\mathrm{PP}}^{\mathrm{sph}}$ is essentially dependent only on S_z

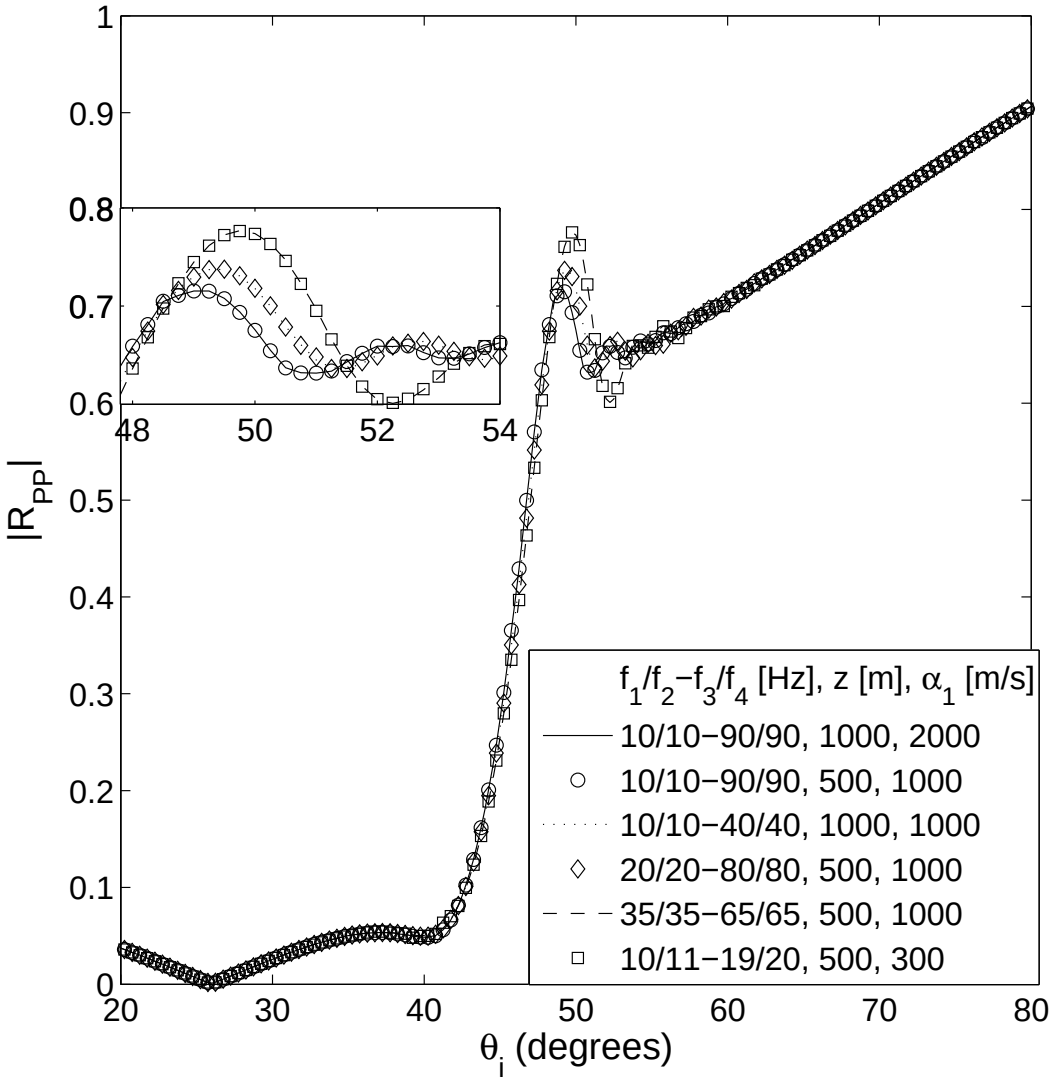

FIG. 6. The six Ormsby wavelet spherical-wave reflection coefficient curves shown in this figure all possess a common value of $\overline{S}_z = \alpha_1/(2z\overline{f})$, namely, 1/50. Note that they track each other closely over most angles. In cases when α_1 varies from the value in Table 1, all other velocities have been similarly scaled so that the underlying plane-wave reflection coefficient curve is unchanged. The inset shows the critical angle region where most variation occurs, and the six curves separate into three pairs of lines. Each pair is characterized by a common value of $B_r \equiv (f_1 + f_2)/(f_3 + f_4)$, and thus the variables $\overline{S}_z$ and B_r control the deviation of the spherical-wave reflection coefficient from its plane-wave analogue.

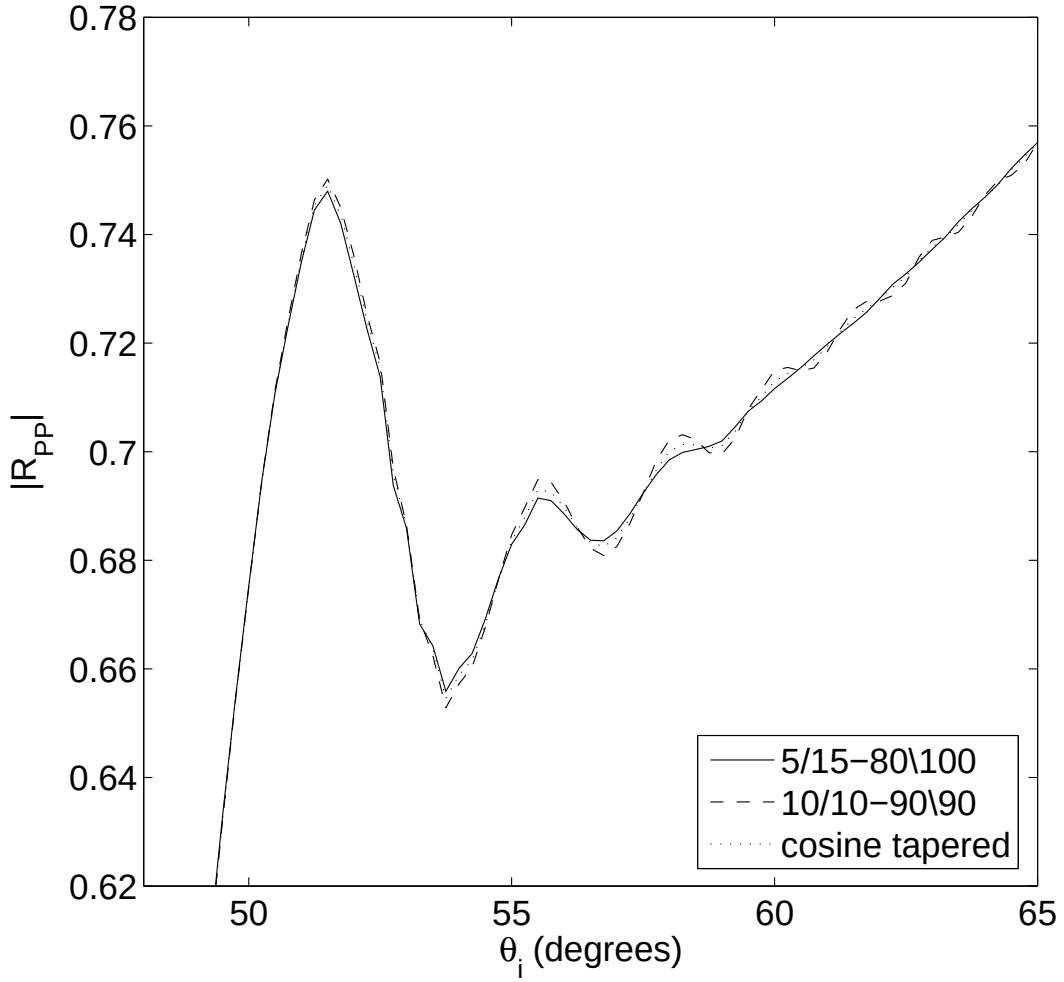

FIG. 7. Three spherical-wave reflection coefficient curves calculated at 500 m depth from Ormsby wavelets with similar bandwidths and average frequencies, namely, a linearly tapered 5/15-80/100 wavelet, a cosine tapered 5/15-80/100 wavelet, and a 10/10-90/90 boxcar wavelet. The axis limits have been adjusted to focus on a region in which there are perceptible differences. Even here the differences are small, suggesting that spherical-wave reflection coefficients are insensitive to the precise edge definitions of Ormsby wavelets.

(or equivalently on $\overline{S}_z = (\sqrt{\pi}/2)S_z$, as shown in Appendix B). By "essentially" we mean that there is deviation on the order of 10^{-3} between similar curves. It is not clear if this is a theoretical or numerical difference. For practical purposes in exploration seismology though, such curves are identical.

Our test of the wavelet approximation can now be phrased as follows: Given values of $\overline{S}_z^{\text{Ricker}}$, or of B_r and $\overline{S}_z^{\text{Ormsby}}$, can we find optimal values of n and S_z^{Rayleigh} such that the Rayleigh reflection coefficient curve gives a good approximation to the Ricker and Ormsby curves.

Selecting S_z

The obvious choice would seem to be to select S_z such that $\overline{S}_z^{\text{Rayleigh}} = \overline{S}_z^{\text{Ormsby or Ricker}}$. However there are other choices one might contemplate. Using the Ormsby wavelet f_1/f_2-f_3/f_4 = 5/15-80/100 Hz, Figure 8 illustrates three representation possibilities for the case of n = 4. First, it is approximated by an f_0 = 23 Hz Rayleigh wavelet. This primarily attempts to reproduce the lower frequencies, as these might be assumed to be more important in reproducing spherical-wave effects. Second, it is approximated by a 40 Hz wavelet, which matches the 50 Hz average frequency of the Ormsby wavelet. (Details of this calculation are given in Appendix B.) This choice also matches values of $\overline{S}_z$ as α_1 and z are unchanged. Finally, it is represented by a 70 Hz wavelet. This represents the upper frequencies of the Ormsby wavelet, and is also a closer match of bandwidth.

Figure 9 below compares the reflection coefficient curve obtained using f_0 = 23, 40, or 70 Hz with that obtained from a numerical calculation using the Ormsby wavelet. This illustrates that setting f_0 equal to the average frequency of the target wavelet provides a good qualitative representation of the reflectivity, even though the wavelets themselves appear substantially different.

Calculations (not shown) also confirm that matching $\overline{S}_z$ provides a good description of the Ricker wavelet reflectivities, although matching values of S_z is reasonable as well.

Selecting n

Selecting S_z is the principal key to representing an arbitrary wavelet's reflection coefficient by that of a Rayleigh wavelet, but the parameter n can still be used to improve the representation.

An example of choosing the optimal value of n is shown in Figure 10. This figure displays reflection coefficient curves for a Ricker wavelet and for eight Rayleigh wavelets, with $n = 1, \ldots, 8$. All nine wavelets share the same value of $\overline{S}_z$. Choosing the best value of n by inspection is somewhat subjective, so the misfit for each n is calculated by an L1 norm (the sum of absolute deviations, $\sum_{i=20^\circ}^{60^\circ} |R_{PP}^{\text{Ormsby}}(\theta_i) - R_{PP}^{\text{Rayleigh}}(n;\theta_i)|$) for a region around the critical angle. This measure assigns the optimal value of $n = 5$, although it is a shallow minimum, and n = 4 and 6 are nearly as suitable.

Would this value of n be optimal in all cases? Some variables that could affect the

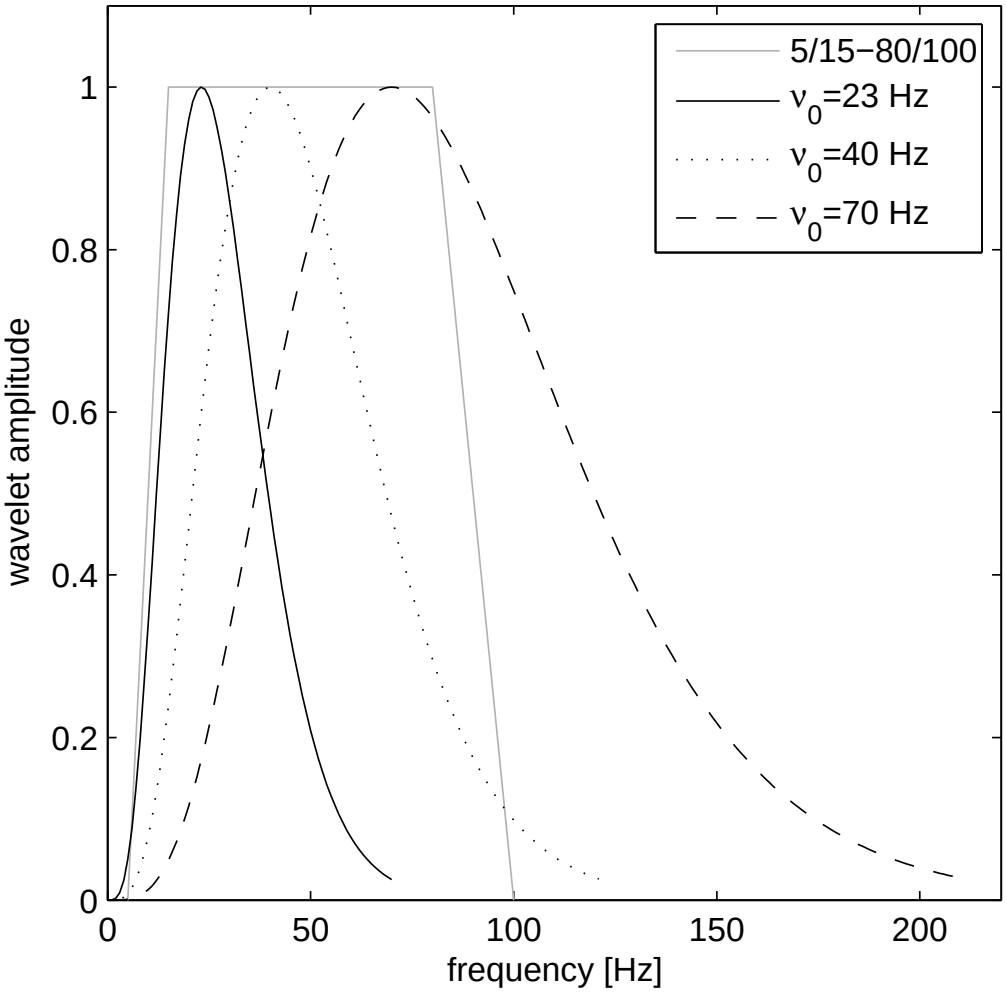

FIG. 8. An Ormsby wavelet and three Rayleigh wavelets (equation 3 with n = 4) which are used to represent it. Two of the wavelets focus on representing the lower or upper Ormsby frequencies. The middle wavelet has the same average frequency as the Ormsby wavelet.

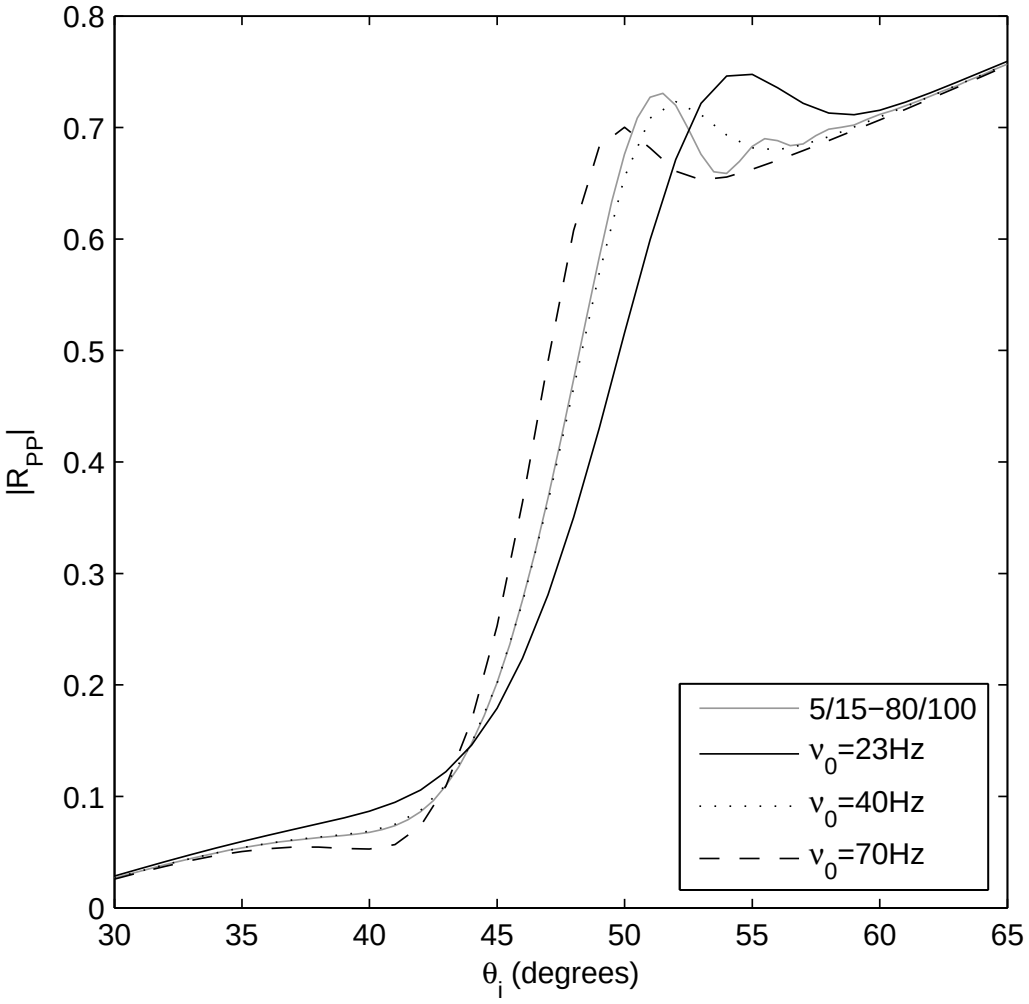

FIG. 9. Four reflection coefficient curves calculated at 500 m for the wavelets in Figure 8. The reflection coefficient of an Ormsby wavelet is best represented by a Rayleigh wavelet bearing the same average frequency.

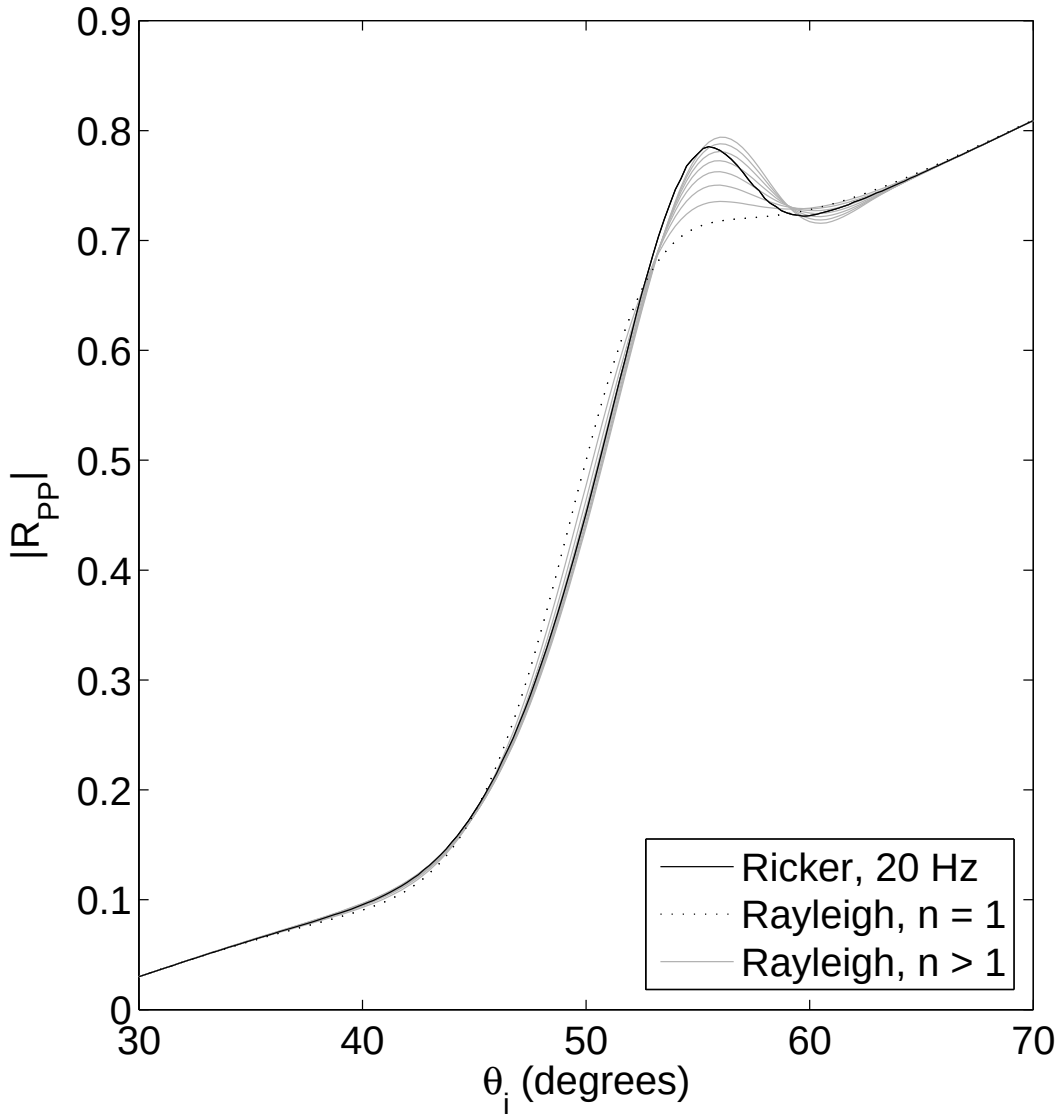

FIG. 10. The dark line is the spherical reflection coefficient curve for the 20 Hz Ricker wavelet at 500 m depth. The remaining curves are for Rayleigh wavelets. Each has a different value of n, but all have the same average frequency as the Ricker wavelet.

choice of n are $\overline{S}_z$, B_r, choice of Ricker vs. Ormsby, and even the earth parameters determining the plane-wave reflection coefficients. We have carried out a number of similar exercises to that of Figure 10 in order to explore dependence of n on these variables. The results are shown in Table 2. The table makes reference to Models I, II, and III. Model I is that given in Table 1. Models II and III are identical to Model I except that $\rho_2 = 2900$ kg/m^3 in Model II and $(\rho_2, \alpha_2) = (2900$ kg/m^3, 2550 m/s) in Model III. As shown in Figure 11, these parameter changes yield significant differences in the plane-wave reflection coefficients, and thus serve as a strong test of the dependence of n on earth parameters. As shown in Table 2, the optimal value of n depends primarily on the choice of wavelet and, in the case of Ormsby wavelets, on B_r as well. Based on these and other calculations, we recommend the choice of $n = 5$ for representing a Ricker curve, and $n = 26B_r$ (rounded) for representing an Ormsby curve. One should recall however that the quality of representation is primarily determined by the choice of S_z, and the choice of n simply refines that representation.

Table 2. The optimal values of the Rayleigh wavelet parameter n used for fitting Ricker and Ormsby wavelets with $\overline{S}_z$ varying over two orders of magnitude, and for models with widely varying plane-wave reflection coefficient curves. Models I, II and III are defined in Figure 11. It is evident that n is only weakly dependent upon $\overline{S}_z$ and on the choice of earth model.

Wavelet			Optimal n value for Rayleigh Wavelet		
Name	B_r	$\overline{S}_z$	Model I	Model II	Model III
Ricker	-	.01	5	5	5
		.1	5	5	5
		1	5	5	≥ 8
Ormsby	1/9	.01	3	4	3
		.1	3	3	3
		.5	3	3	4
Ormsby	1/4	.01	7	≥ 8	7
		.1	6	6	6
		.5	6	6	≥ 8

To summarize, one can observe from Figures 9 and 10 that, given appropriate selections of S_z and n, Rayleigh reflection coefficient curves provide a strong qualitative estimate of $R_{\text{PP}}^{\text{sph}}$ for Ormsby wavelets and a nearly quantitative estimate for Ricker wavelets.

Efficiency

Table 3 displays times required to carry out the calculation of a single point for a reflection coefficient curve. Note that the timing of the Rayleigh wavelet calculations by the semi-analytical method depend only on $\overline{S}_z$ and n, while the Ricker and Ormsby wavelet calculations, based on the method of Haase (2004a), can have different timing values for the same value of $\overline{S}_z$, depending on the individual definitions of α_1, z and $f(\omega)$. Thus these numbers represent a rough sampling. It is also interesting that the execution time of one method increases with $\overline{S}_z$, and the other decreases. This emphasizes the fact that the two calculation methods involve substantially different approaches.

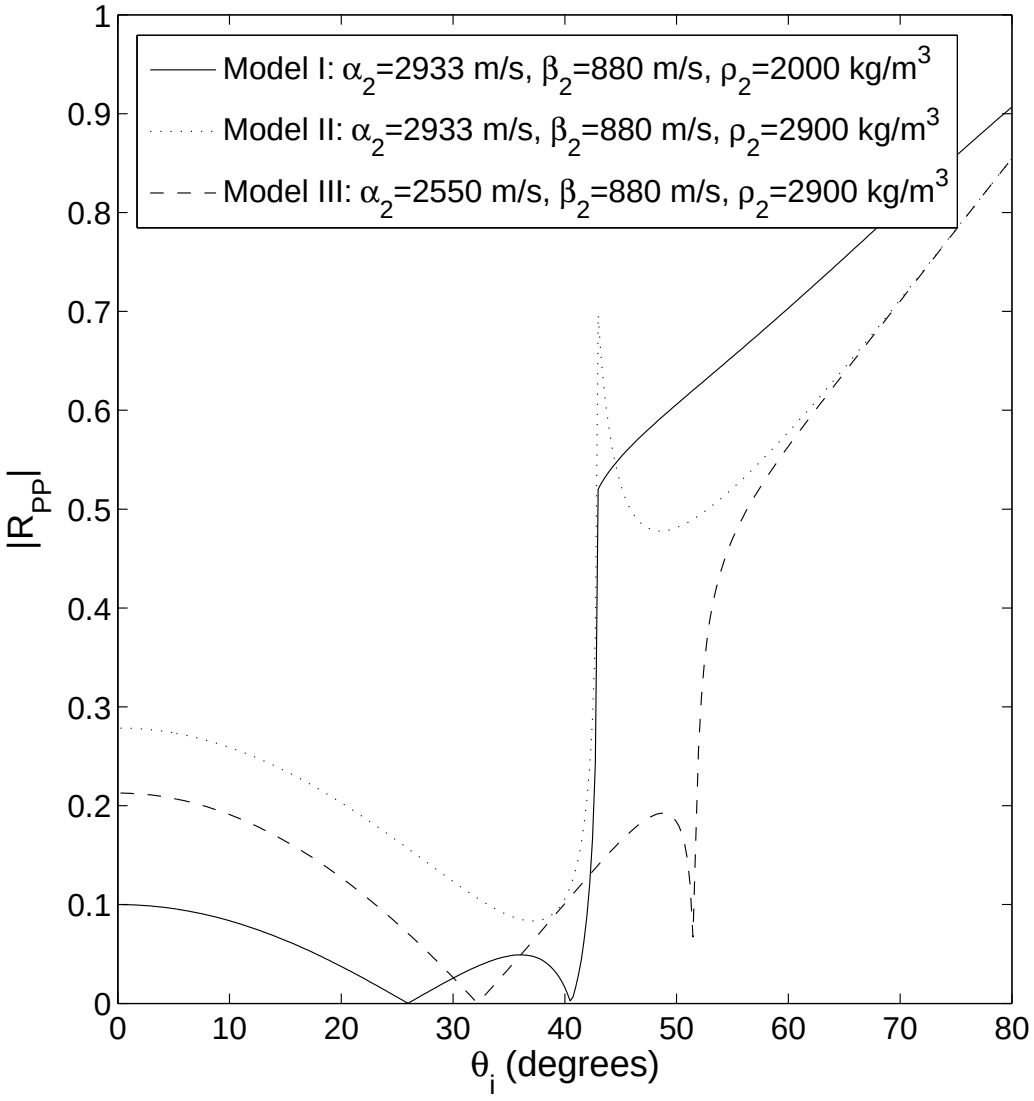

FIG. 11. Three different plane-wave reflection coefficient curves. The solid curve is for the earth parameters of Table 1. The dotted curve is the same except that $\rho_2 = 2900$ kg/m^3. The dashed curve is also for the same parameters as in Table 1 except that now $\rho_2 = 2900$ kg/m^3 and $\alpha_2 = 2550$ m/s. They are intended to display widely varying Class I behaviors in order to see whether the optimal value of n is model-dependent. Results collected in Table 2 suggest it is not.

Table 3. Times in seconds required to calculate a point of the spherical-wave reflection coefficient curve. The Ricker and Ormsby results are for a FORTRAN77 code, the Rayleigh results are for a Java applet.

Wavelet	$\overline{S}_z = .01$	$\overline{S}_z = .1$	$\overline{S}_z = .5$ or 1
Ricker	67.5	4.9	.15
Rayleigh, $n = 5$	0.058	0.058	0.071
Ormsby, $B_r = 1/9$	71	.45	.16
Rayleigh, $n = 3$	0.032	0.032	0.038

It is clear that $R_{\rm PP}^{\rm sph}(\theta_i)$ calculations based on equation 21 are fast enough to be executed interactively. They are a promising basis for large scale AVO modeling or inversion of seismic data. In addition, if a calculation has been previously executed, and one wishes to recalculate using a different value of $\Delta\alpha/\alpha$, $\Delta\beta/\beta$, $\Delta\rho/\rho$, or β/α, it is only necessary to recalculate the plane-wave $R_{\rm PP}$, as W_n will be unchanged and a stored version can be used. This further decreases the calculation time by another *two orders of magnitude*. This efficiency has been captured in a Java applet implementation of this method, publicly available at www.crewes.org (via the "Explorers" link). In this application, changing a variable that requires a recalculation of W_n typically requires a few seconds of delay, while changing a variable that requires only recalculation of $R_{\rm PP}$ results in an instantaneous response. This extra efficiency is a unique feature of the equation 21 method of calculating $R_{\rm PP}^{\rm sph}$, and would be of considerable value in AVO inversion.

CONCLUSIONS

We have shown that, for the Rayleigh wavelet, one can obtain a simplified expression for spherical-wave reflection coefficients. These reflection coefficients show behavior similar to that obtained from more traditional wavelets. Using simple prescriptions, they can be used to qualitatively represent Ormsby wavelets and quantitatively represent Ricker wavelets. Similar principles would allow them to represent other wavelets as well. These calculations are nearly exact, with the main restriction being the form of the wavelet.

This new approach is admittedly not as flexible as the numerical approach of Haase (2002, 2003, 2004a), which can not only be easily extended to other wavelets, but to converted waves Haase (2004a), viscoelastic media (Haase, 2004b), and anisotropic media (Haase and Ursenbach, 2005) as well. However the case of PP-reflections in isotropic, elastic media is central to exploration seismology. Furthermore, the unique efficiencies of this method make it feasible to implement in interactive software, and suggest that it is a promising method for use in supercritical AVO modeling. Spherical-wave reflection coefficient calculations, which formerly have been used only in special instances, can now be implemented routinely.

ACKNOWLEDGEMENTS

The authors gratefully acknowledge the assistance of the CREWES Sponsors.

REFERENCES

Aki, K., and Richards, P. G., 1980, Quantitative seismology, Theory and Methods: Volume 1: W. H. Freeman and Company.

Bortfeld, R., 1962, Reflection and refraction of spherical compressional waves at arbitrary plane interfaces: Geophys. Prosp., **10**, No. 04, 517–538.

Cagniard, L., 1939, Réflection et réfraction des ondes seismiques progressives: Gauthier-Villars.

Downton, J. E., 2005, Seismic parameter estimation from AVO inversion: Ph.D. thesis, University of Calgary, available at www.crewes.org.

Downton, J. E., and Ursenbach, C., 2006, Linearized amplitude variation with offset (AVO) inversion with supercritical angles: Geophysics, **71**, No. 5, E49–E55.

Erdelyi, A., 1954, Tables of Integral Transforms, vol. 1: McGraw-Hill.

Furlong, J. R., Westbury, C. F., and Phillips, E. A., 1994, A method for predicting the reflection and refraction of spherical waves across a planar interface: Journal of Applied Physics, **76**, 25–32.

Haase, A., 2002, Plane waves, spherical waves and angle-dependent P-wave reflectivity in elastic VTI-models, *in* 71st Ann. Internat. Mtg, Soc. of Expl. Geophys., 304–307.

Haase, A. B., 2003, Approximation errors in AVO-analysis and inversion, *in* 2003 CSPG / CSEG National Convention, Canadian Soc. of Expl. Geophys.

Haase, A. B., 2004a, Spherical wave AVO modeling of converted waves in elastic isotropic media, *in* 2004 CSEG National Convention, Canadian Soc. of Expl. Geophys.

Haase, A. B., 2004b, Spherical wave AVO modeling of converted waves in isotropic media, *in* 73rd Ann. Internat. Mtg, Soc. of Expl. Geophys., 263–266.

Haase, A. B., and Ursenbach, C., 2005, Spherical-wave AVO-modeling in elastic and anelastic transversely isotropic (VTI) media, *in* 74th Ann. Internat. Mtg, Soc. of Expl. Geophys., 316–319.

Hilterman, F. J., Schuyver, C. V., and Sbar, M., 2000, AVO examples of long-offset 2-D data in the Gulf of Mexico: The Leading Edge, **19**, No. 10, 1200–1213.

Hosken, J. W. J., 1988, Ricker wavelets in their various guises: First Break, **06**, No. 01, 24–33.

Hubral, P., and Tygel, M., 1985, Transient response from a planar acoustic interface by a new point-source decomposition into plane-waves: Geophysics, **50**, No. 05, 766–774.

Hubral, P., and Tygel, M., 1989, Analysis of the Rayleigh pulse (short note): Geophysics, **54**, No. 05, 654–658.

Kanasewich, E. R., 1973, Time Sequence Analysis in Geophysics: University of Alberta Press.

Krail, P. M., and Brysk, H., 1983, Reflection of spherical seismic waves in elastic layered media: Geophysics, **48**, No. 06, 655–664.

Lamb, H., 1904, On the propagation of tremors over the surface of an elastic solid: Phil. Trans. Roy. Solc. (London) A, **203**, 1–42.

MacDonald, C., Davis, P. M., and Jackson, D. D., 1987, Inversion of reflection traveltimes and amplitudes: Geophysics, **52**, No. 05, 606–617.

Sommerfeld, A., 1909, Über die Ausbreitung der Wellen in der drahtlosen Telegraphie: Ann. Physik, **28**, 665–736.

Tygel, M., and Hubral, P., 1984, Transient representation of the Sommerfeld-Weyl integral with application to the point source response from a planar acoustic interface: Geophysics, **49**, No. 09, 1495–1505.

van der Baan, M., and Smit, D., 2006, Amplitude analysis of isotropic P-wave reflections: Geophysics, **71**, No. 6, C93–C103.

Wang, Y., 1999, Approximations to the Zoeppritz equations and their use in AVO analysis: Geophysics, **64**, No. 6, 1920–1927.

APPENDIX A

We consider the limit of *decreasing* S for equations 21-26.

First we consider the $\cos\theta \neq \cos\theta_i$. In this case B, C, $\overline{\tau}$ and $\overline{T}$ are all non-vanishing in the limit. Thus the S^{n+2} factor will cause W_n to vanish.

Next we consider the case $\cos\theta = \cos\theta_i \neq 0$. Again C and $\overline{T}$ are non-vanishing, but $\overline{\tau}$ vanishes as $\sqrt{S}$, so that $BP_n(\overline{T}/\overline{\tau})$ and $P_{n+1}(\overline{T}/\overline{\tau})$ diverge as $(1/\sqrt{S})^{n-1}$ and $(1/\sqrt{S})^{n+1}$ respectively. The former of these can be neglected, and W_n will then diverge as $1/\sqrt{S}$.

Finally we consider the remaining case, $\cos\theta = \cos\theta_i = 0$. Setting this condition and then taking the limit of $S \to 0$ yields $-i(n+2)/(nS)$ which diverges as $1/S$.

The real and imaginary components of W_n are bounded by the envelope. Thus, because the real part is normalized to 1 and the imaginary part to zero, the weighting function must act as a delta function in the limit of vanishing spherical effects, i.e., $\lim_{S\to 0} W_n(\theta, \theta_i, S) = \delta(\cos\theta - \cos\theta_i)$.

APPENDIX B

The average frequency of a wavelet is given by

$$\overline{f} = \frac{\int_0^\infty f w(f) df}{\int_0^\infty w(f) df}. \tag{28}$$

Applying this to the wavelet definitions in equations 3 and 27 yields

$$\overline{f}_{\text{Rayleigh}} = \frac{n+1}{n} f_0^{\text{Rayleigh}}, \tag{29}$$

$$\overline{f}_{\text{Ricker}} = \frac{2 f_0^{\text{Ricker}}}{\sqrt{\pi}}, \tag{30}$$

while application to the Ormsby wavelet gives

$$\overline{f}_{\text{Ormsby}} = \frac{(f_1^2 + f_1 f_2 + f_2^2) - (f_3^2 + f_3 f_4 + f_4^2)}{3(f_1 + f_2 - f_3 - f_4)}. \tag{31}$$

Mimicking the average frequency of the target wavelet can then be accomplished by solving for f_0^{Rayleigh} from $\overline{f}_{\text{Rayleigh}} = \overline{f}_{\text{Ricker}}$ or from $\overline{f}_{\text{Rayleigh}} = \overline{f}_{\text{Ormsby}}$.

The quantity $\overline{S}_z$ is defined as $\alpha_1/(z\overline{f})$, so that if α_1 and z are held constant, then matching $\overline{f}$ is equivalent to matching $\overline{S}_z$.